Interband cascade lasers with advanced waveguides operating in the 3-4 μm wavelength region

Jeremy. A. Massengale, [a,b,+,*] Yixuan Shen, [a,+] Rui Q. Yang, [a,*] Tetsuya D. Mishima, [b] and Michael B. Santos [b]

[a]School of Electrical and Computer Engineering, University of Oklahoma, Norman, OK
[b]Homer L. Dodge Department of Physics and Astronomy, University of Oklahoma, Norman, OK USA 73019

Abstract. We report the first implementation of an advanced waveguide structure, consisting of GaSb separate confinement layers, n-doped InAs/AlSb superlattice intermediate cladding layers, and n^+-doped $InAs_{0.91}Sb_{0.09}$ plasmon-enhanced cladding layers for GaSb-based interband cascade lasers (ICLs) with lasing wavelengths in the 3-4 μm wavelength region. This advanced waveguide configuration for ICLs can have improved thermal dissipation and enhanced optical confinement. Although the grown ICL wafers had significant layer thickness deviations from the designed values, devices made from them exhibited room temperature (RT) threshold current densities as low as 148 A/cm^2 and high voltage efficiencies (e.g., 69%), implying a considerable potential of the advanced waveguide configuration for further improved device performance. A comparative study among the devices revealed how the structural variations could affect the carrier transport and threshold voltage, providing useful guidance for future research. Additionally, the ICLs tested here had characteristic temperatures of nearly 60 K, which is the highest among RT ICLs with similar lasing wavelengths, supporting the further development of the advanced waveguide in GaSb-based ICLs operating in this wavelength range.

Keywords: Interband cascade lasers, mid-infrared semiconductor lasers, type-II quantum well heterostructures, III-V materials, optical waveguides.

[+] J.M. and Y.S. contributed equally to this work.
*****Corresponding authors**,** E-mail: massengalej@ou.edu, Rui.q.Yang@ou.edu

1 Introduction

Interband cascade lasers (ICLs) [1] based on a type-II quantum well (QW) active region have attracted much interest over the years, in large part due to their low power consumption. Their operation hinges on two key features: interband transitions in type-II quantum wells and a cascade configuration, which enhances the total gain (per current density) [1-5] and was first developed for quantum cascade lasers (QCLs) [6]. However, the ICL stands apart from the QCL in that its interband transition nature makes it immune to phonon scattering, a key loss mechanism for the QCL, which allows the ICL to lase with a much lower threshold current density (J_{th}). These features of the ICL are ideal for a host of practical applications in the mid-infrared (MIR) including gas/chemical sensing, imaging, industrial process control, and free-space optical communication [7-11]. The GaSb-based ICLs have demonstrated efficient room temperature (RT) operation in the 3-6 μm range but exhibited performance below their InAs-based counterparts beyond 6 μm due partially to limited effort and the difficulties associated with the waveguide traditionally used [4-5,12-13]. The typical waveguide used in a GaSb-based ICL consists of two Te-doped GaSb

separate confinement layers (SCLs) surrounding the cascade active region, wrapped by two n-type doped InAs/AlSb superlattice (SL) cladding layers, which have a low thermal conductivity and a small contrast in refractive index with the cascade region. On the other hand, the InAs-based ICLs have utilized a heavily n^+-type doped InAs plasmon-enhanced cladding layer, instead of the InAs/AlSb SL, to improve the optical confinement and the overall thermal conductivity of the device [14-17], resulting in the wavelength coverage of ICLs extending to 11.2 μm. For InAs-based ICLs operating near 4.6 μm, it was later shown that an advanced waveguide structure utilizing hybrid cladding layers, which combines a relatively thin InAs/AlSb SL intermediate (Int.) cladding layer with the n^+-type doped InAs plasmon cladding, enabled enhanced device performance by reducing the free-carrier loss and yielding improved optical confinement within the cascade active region [18]. This advanced waveguide was later shown to improve performance in long wavelength InAs-based ICLs emitting between 10-13 μm [19-20] and was also explored in GaSb-based ICLs operating between 3.8 and 6.1 μm [21-22] where the plasmon-enhanced cladding layer in the latter is composed of n^+-type doped $InAs_{0.91}Sb_{0.09}$. Here we report a study of several GaSb-based ICLs which incorporate this advanced waveguide structure [23] and emit in the 3-4 μm wavelength region. Despite structural deviations originating from the MBE growth, the continuous wave (cw) and pulsed performance of these broad area (BA) ICLs display similar performance to, and in some cases exceed, that of other GaSb-based ICLs which utilize the conventional waveguide and emit near a similar wavelength. Furthermore, a performance comparison between them shows the important impact of smooth carrier transport on the voltage efficiency.

2 Design, Growth, and Fabrication

Three wafers (Y082L, Y086L, and Y087L) were grown as a series of GaSb-based ICLs with designs employing the advanced waveguide structure. Some preliminary results of ICLs made from wafer Y082L were reported in the SPIE Conference Proceedings [23]. Since those results are part of a series of experiments on related structures, they are included for comparison and completeness in this work. All three ICL wafers have 6 cascade stages (N_c) where each W-QW active region consists of a nominally identical layer sequence of AlSb/InAs/$Ga_{0.6}In_{0.4}Sb$/InAs/AlSb, with layer thicknesses of 25/16.5/28/14/12 Å in the growth direction, for a targeted lasing wavelength near 3.3 μm at RT. The ICL wafers had GaSb SCLs

doped with Te to a level of 2.7×10^{17} cm^{-3}, each with a thickness of 2100 Å. The ICL wafers included 1 μm thick (bottom) and 0.7 μm thick (top) n^{+}-doped $InAs_{0.91}Sb_{0.09}$ plasmon cladding layers with a doping level of 3.2×10^{19} cm^{-3} and 0.75 μm (bottom and top) n-doped (1.5×10^{17} cm^{-3}) InAs/AlSb SL Int. cladding layers. The ICL wafers Y082L and Y086L share an identical design, while in Y087L, the thickness of the GaSb layers in the hole injector were increased by ~10% to widen the interband tunneling window for smooth carrier transport at a given voltage. The overall structure design is shown in Fig. 1a which includes thin InAs/AlSb connection regions between the main waveguide functional segments.

The ICL wafers were grown by molecular beam epitaxy (MBE) using a Veeco GENxplor with As and Sb supplied by valved cracking sources. The crystalline quality of the grown ICL wafers was assessed using x-ray diffraction (XRD) and the surface morphology was characterized by differential-interference-contrast microscopy (DIC). From the DIC images, typical oval hillock defects were observed – common to III-V ICL growth, but with little background surface roughness. The average surface defect density of these ICL wafers ranged from 1.0×10^{3} to 1.4×10^{4} cm^{-2} which are within acceptable limits for reasonable device performance. A representative XRD pattern from symmetric ω-2θ scans normal to the (004) plane is shown in Fig. 1b. In Y082L, an average tensile strain for the InAs/AlSb SL Int. cladding of 0.13% in the growth direction (biaxial compressive strain) was observed, while both Y086L and Y087L had an average tensile strain of 0.045%, indicating a slightly superior crystal quality. From analysis of the XRD measurements, deviations from the intended design were observed. The MBE growth deviations mainly affected the thicknesses of the cascade active region and the InAs/AlSb SL Int. cladding layers. In Y082L, the cascade active region and the SL Int. cladding layers were approximately 14.5% and 9.6% thinner than expected. Conversely, in Y086L and Y087L these layers showed deviations in the opposite direction and were about 13.4% and 16.9% thicker than intended. Table I lists the structural differences as well as performance features of the corresponding broad-area devices at 300 K, along with their respective maximum cw operating temperatures T_{cwmax}.

Table I. summary of layer thickness variations and device performance features at 300K

wafer	Thickness variations		Pulsed	Pulsed J_{th}	Pulsed V_{th}	η_v (%)	T_{cwmax}
	SL	cascade	λ (μm)	(A/cm^2)	(V)		(K)
Y082L	-9.6%	-14.5%	3.285	179	5.31	42.6	242
Y086L	16.22%	13.38%	3.824	154	3.02	64.4	260
Y087L	17.50%	13.40%	3.812	148	3.24	60.2	260

The potential impact that these structural differences can have on the measured electrical and optical properties such as threshold voltage V_{th}, voltage efficiency η_v, and emission wavelength λ will be presented and discussed later in detail. First, we will evaluate the impact on the optical confinement factor in the cascade active region (Γ) and the internal loss due to free-carrier absorption (α_i) based on waveguide simulations. Fig. 2 shows the calculated optical modal profile and refractive index for these ICL wafers based on the intended design parameters, with a targeted emission wavelength of λ = 3.30 μm, which result in Γ = 21.4% and α_i = 5.13 cm^{-1}. Thus, the required threshold gain g_{th} due to the free-carrier absorption without other possible losses is 42.5 cm^{-1} for a 3-mm-long cavity ICL. In Y082L, both the SL cladding and the cascade active region are thinner than designed, leading to a decrease in the optical confinement to Γ = 19.1% at a wavelength of λ = 3.30 μm, as shown in Fig. 3 (red). The simulation also suggests an increase in both the free-carrier loss and the required threshold gain to 5.83 cm^{-1} and 51 cm^{-1}, respectively. This is because the thinner SL intermediate cladding layer allows more of the optical wave to leak into the plasmon cladding layer, resulting in an increase in the free-carrier absorption, while the thinner cascade active region results in a smaller overlap between the optical field and the cascade active region, which reduces the optical confinement. On the other hand, for Y086L, the experimentally observed lasing wavelength of 3.824 μm at 300 K is significantly longer than the targeted wavelength, which needs to be adopted in the simulation (Fig. 3 green). The thicker SL cladding and cascade active regions lead to an increase in Γ = 22%, but the red-shifted wavelength causes an increase in α_i =6.52 cm^{-1}. Combining the two factors, the threshold gain g_{th} would increase to 48 cm^{-1} for Y086L, which is slightly lower than that for Y082L. The waveguide simulation results for Y087L are similar to those of Y086L. Hence, based on the waveguide simulation, the threshold current density at 300 K in devices made from Y086/87L should be slightly lower than that in devices made from wafer Y082L.

To investigate the effects of these growth deviations and evaluate how the devices perform in comparison with each other and to the waveguide simulations, the grown ICL wafers were fabricated into devices with 100-μm-wide (e.g., Y082LBA1-3F, Y086LBA1-1H, Y086LBA1-2A, Y086LBA1-2B and Y087LBA1-1H) and 150-μm-wide (e.g., Y082LBA1-3H, Y086LBA1-1F, Y086LBA1-2C, Y086LBA1-2D, and Y087LBA1-1F) broad area (BA) mesas using standard UV contact photolithography and wet chemical etching. The wafers were left unthinned and cleaved into approximately 2-mm-long (Y086LBA1-2A, Y086LBA1-2B, Y086LBA1-2C, and

Y086LBA1-2D) and 3-mm-long (all other devices) laser bars without facet coatings, which were mounted epi-side up on copper heat sinks for testing.

3 Performance of ICL Devices

Despite the growth deviations previously discussed, BA devices from all three ICL wafers lased in both cw and pulsed modes with reasonable threshold current densities as depicted in Fig. 4. These values are comparable to the those of state-of-the-art ICLs at similar wavelengths and will be discussed in detail below. However, at temperatures below 330 K, the threshold voltages for devices from wafer Y082L were noticeably higher (Fig. 4) than those from the other two ICL wafers, leading to relatively low voltage efficiencies, such as 42.6% at 300 K for example (Table I). This implies that the reduction of layer thicknesses associated with the growth deviations in wafer Y082L seriously affected energy level alignments across the QWs and thus rendered the carrier transport less smooth than designed. On the other hand, the unintentional increase of layer thicknesses in wafers Y086/87L did not significantly affect the carrier transport, as reflected in Fig. 4 by the low threshold voltages and reasonable voltage efficiencies (e.g., 64% at 300 K in Table I). Nevertheless, due to the growth deviations, the emission wavelengths for these ICL devices exhibited some considerable differences from the expected design as shown in Fig. 5. The ICLs from wafer Y082L spanned a wavelength range from 2.9 to 3.4 μm when the temperature was varied from 80 to 370 K, while ICLs from wafers Y086/87L spanned a wavelength range from 3.35 to 3.92 μm under a similar temperature variation. At room temperature their pulsed lasing wavelengths were about 3.28 μm and 3.82 μm for devices from Y082L and Y086/87L, respectively. In the temperature range from 80 to 300 K, the threshold current density and voltage were substantially lower in ICLs from wafers Y086/87L compared to wafer Y082L, which resulted in about a 20 K higher maximum cw operating temperature for wafers Y086/87L as shown in Fig. 4 and Table I. The lower J_{th} at 300 K in devices from wafers Y086/87L is qualitatively consistent with the slightly lower threshold gain based on the simulation results in Fig. 3. Detailed characteristics for representative devices from each of the ICL wafers will be presented and discussed in the following subsections.

3.1 Y082L Performance

In cw mode, a representative 100-μm-wide device from the first ICL wafer, Y082LBA1-3F, lased at 80 K with an emission wavelength of λ = 2.89 μm, a J_{th} = 10.5 A/cm^2, and a V_{th} = 7.4 V. The corresponding voltage efficiency of 35% is relatively low, indicating a problem related to the carrier transport. Y082LBA1-3F continued to operate up to 242 K in cw mode, with an emission wavelength of λ = 3.25 μm and a J_{th} of 165 A/cm^2. A representative 150-μm-wide device, Y082LBA1-3H, exhibited similar 80 K performance and operated up to a maximum cw temperature of 225 K with an emission wavelength of λ = 3.21 μm and a J_{th} of 106.9 A/cm^2. The cw operating temperature difference between the two devices is due to the increased thermal load in device H, which requires a higher injection current to achieve lasing due to the wider laser ridge. The difference in thermal load is reflected by the difference in the specific thermal resistance values of 72.1 and 80.7 Kcm^2/kW. Fig. 6 shows a representative plot of the cw current-voltage-light (IVL) characteristics for Y082LBA1-3F. Y082LBA1-3F reached a source-limited cw output power at 80 K of 121.5 mW/facet at an injection current of 500 mA with an extracted external quantum efficiency (EQE) of 131%, indicating the cascaded emission of photons in the ICL, and dropped to 27% at 240 K with a cw output power of 4.4 mW/facet. Y082LBA1-3H showed similar performance, with a source-limited cw output power at 80 K of 116 mW/facet and a corresponding EQE of 147%, dropping to 32% at 225 K with a cw output power of 1.9 mW/facet.

In pulsed operation, (5kHz repetition rate and 1 μs pulse width) the Y082LBA1-3F and Y082LBA1-3H devices were able to lase up to 370 K with a J_{th} = 773 A/cm^2 and 360 K with a J_{th} = 600 A/cm^2, respectively, with the temperature dependent pulsed spectra for Y082LBA1-3F shown in Figure 7. Another device with a 1.5 mm cavity length and a 100 μm wide ridge, Y082BA1-1C, was operated up to 390 K and was then damaged with the high pulsed current. Y082LBA1-3F lased in pulsed mode at RT with an emission wavelength of λ = 3.28 μm and a J_{th} = 181 A/cm^2, while Y082LBA1-3H lased at a similar wavelength with a J_{th} = 177 A/cm^2. These J_{th} values are somewhat similar to a 5-stage GaSb-based ICL which utilized the traditional waveguide and exhibited RT lasing at λ = 3.6 μm with a J_{th} = 134 A/cm^2[24]. As ref. [24] points out, the threshold tends to increase at even shorter wavelengths, rising above 200 A/cm^2 for devices emitting below 3.1 μm. However, the threshold voltages from devices made from Y082L were relatively high (>5 V) with low voltage efficiencies as illustrated in Figs. 4 and 6, as well as in Table I, suggesting unsmooth carrier transport. This might be caused by the substantial reductions

in layer thicknesses from the intended design, which could narrow the interband tunneling window between the electron and hole injectors [2, 25] and consequently would require a higher voltage to open and widen the tunneling window. Nevertheless, these ICLs were able to lase in pulsed mode at high temperatures (up to 390 K) with characteristic temperature (T_o) values in pulsed mode of 59.5 K and 58.0 K in the temperature range of 200-360 K, respectively, which is higher than previously reported values (T_0~45-55 K) from early RT ICLs [5,12] with similar lasing wavelengths.

3.2 Y086L Performance

Devices from ICL wafer Y086L have thicker layers in both the cascade active region and the InAs/AlSb SL Int. cladding layers, compared to the intended designed, as previously discussed in Section 2. In cw mode, representative devices from the second ICL wafer, Y086LBA1-1H (100-μm-wide) and Y086LBA1-1F (150-μm-wide), lased at 80 K with emission wavelengths of λ = 3.36 and 3.37 μm, respectively where the small difference in wavelength was due to the possible non-uniformity of material and different sizes of the two devices. They had similar threshold current densities of J_{th} = 7 and 6.9 A/cm^2, about 30% lower than those from Y082L, indicating a reduced Shockley-Read-Hall (SRH) recombination that is consistent with the lower defect density observed in this wafer. The emission wavelength at 80 K was longer than the intended RT design of 3.30 μm, which is qualitatively in agreement with the observed thickness increases according to the XRD measurements discussed in Section 2. These devices had reduced threshold voltage values of V_{th} = 3.25 (corresponding to a η_v of 68%) and 3.59 V, respectively, about a 50% reduction compared to devices from Y082L, implying that the carrier transport was improved. The 2-mm-long cavity length devices from this ICL wafer (Y086LBA1-2B and Y086LBA1-2C) operated up to 260 K and 250 K, respectively, in cw mode with emission wavelengths of λ= 3.772 and 3.767 μm, J_{th} = 152.5 and 103.3 A/cm^2, and V_{th} = 3.12 and 3.01 V, respectively. Fig. 8 shows the cw current-voltage-light (IVL) characteristics of Y086LBA1-2B, which is a representative device among the many devices tested and listed in Fig. 4. Y086LBA1-2B reached a peak EQE at 80 K of 210%, which subsequently decreased with increased heat-sink temperature to 42% at its maximum cw operating temperature. The device could be operated in cw mode at a few degrees higher than 260 K according to its threshold characteristics in Fig. 8, but was not pushed to the

higher temperature in order to avoid possible accidental damage. Other devices from Y086L showed similar performance. The differences in the measured EQE and maximum cw operating temperature for devices from Y086L and Y082L are qualitatively consistent with the substantially reduced threshold current density and lower threshold voltage with improved carrier transport for devices from Y086L as shown in Fig. 4.

In pulsed operation, (5kHz repetition rate and 1 μs pulse width) the Y086LBA1-1H and Y086LBA1-1F devices were able to lase up to 360 K and 340 K. The results from Y086LBA1-1H shown in Fig. 9, are also representative of the other devices tested. At their maximum operating temperature, these devices had emission wavelengths of 3.90 and 3.89 μm, and threshold current densities of J_{th} = 771.3 and 443.8 A/cm^2, respectively. At RT, these devices lased at 3.82 μm with nearly equal threshold current densities of J_{th} = 154.7 and 153.8 A/cm^2, respectively, about 23 A/cm^2 lower than for devices from wafer Y082L. This emission wavelength at RT was red-shifted somewhat severely, by about 0.5 μm from the intended design value of 3.30 μm due to the growth deviations. Their V_{th} values of 3.02 and 3.06 V, respectively, lead to voltage efficiencies of about 64.4% and 63.6%, which is more than 20% higher compared to devices from Y082L but less than that of around 70% observed in BA GaSb-based ICLs with the traditional waveguide operating at λ = 3.6 μm at RT[26]. This indicates that there may be somewhat unsmooth carrier transport in the ICLs presented here, which would be reflective of the deviations in the growth and imperfect metal contact. However, in the ICLs from Ref. [26], techniques to enhance the thermal management of the ICLs such as thinned substrates and reduced duty cycles were implemented. The pulsed operation of Y086LBA1-1H and Y086LBA1-1F could be extended to slightly higher temperatures by decreasing the duty cycle, as expected from observable heating effects with high current pulses at the 0.5% duty cycle. By using pulsed current injection at a duty cycle of 0.1% the two BA ICLs were operated up to 380 K and 370 K, respectively.

The devices from ICL wafer Y086L had T_o values that ranged from 46.5-48.9 K in the temperature range of 200-360 K, which were somewhat smaller than for devices from ICL wafer Y082L. Although the performance at 80 K for devices from Y086L was superior to those from Y082L, both their J_{th} and V_{th} values exceeded those of devices from Y082L at elevated temperatures, as reflected in Fig. 4. This is likely due to the significantly longer emission wavelength from the intended design at 300 K and the associated changes in the optical parameters

for these ICLs based on the discussion related to Fig. 3. When the emission wavelength at elevated temperatures approaches the plasmon wavelength (λ_p) of the n^+-doped $InAs_{0.91}Sb_{0.09}$ plasmon cladding layers, the free-carrier absorption loss will sharply increase, which can impact the device performance. For example, at the doping level used for the plasmon cladding in these devices, the estimated λ_p = 6.47 μm. At an emission wavelength equal to that of Y082L at RT (λ = 3.28 μm), the estimated free-carrier loss for a bulk layer of $InAs_{0.91}Sb_{0.09}$ is α_i = 427.7 cm^{-1}, while at a wavelength equal to that of Y086L at RT (λ = 3.83 μm), the estimated free-carrier loss is α_i =602.7 cm^{-1}, which is about 41% larger.

3.3 Y087L Performance

Devices from ICL wafer Y087L have thicker layers in both the cascade active region and the InAs/AlSb SL Int. cladding layers, compared to the intended designed, as previously discussed in Section 2. Compared to devices from Y086L, those from Y087L (Y087LBA1-1H and Y087LBA1-1F) consistently showed a slightly lower cw threshold current density of J_{th} = 6.3 and 6.4 A/cm^2, respectively, implying a further reduction in the SRH recombination, consistent with the lower defect density observed in wafer Y087L, compared to Y086L. They lased with cw emission wavelengths of 3.36 μm and 3.35 μm at 80 K that were similar to those of devices from Y086L, but with slightly reduced threshold voltages of V_{th} = 3.42 and 3.22 V (corresponding to a η_v of 69%), respectively. Representative devices from this ICL wafer, 100- μm-wide device Y087LBA1-1H and 150- μm-wide device Y087LBA1-1F, showed comparable maximum cw operating temperatures to those from Y086L of 260 K and 252.5 K, respectively. They had emission wavelengths of λ = 3.8 and 3.78 μm, J_{th} = 146.7 and 123.3 A/cm^2, and V_{th} = 2.96 and 2.62 V, respectively. Overall, the cw lasing characteristics for devices from Y087L exhibit slightly better performance than those from Y086L, which may be reflective of the slight increase in the GaSb layer thicknesses in the hole injector, intended to improve the carrier transport in these devices, but could also be due to somewhat better material quality with a reduced defect density. Fig. 10 shows the cw current-voltage-light (IVL) characteristics of Y087LBA1-1H, which is a representative device among the many devices tested and listed in Fig. 4. Y087LBA1-1H reached a peak EQE at 80 K of 217%, which subsequently decreased with increased heat-sink temperature to 76% at 250 K. Other devices from Y087L showed similar performance. Once again, the differences in the measured EQE and maximum cw operating temperature for devices from Y087L

and Y082L are related to the superior lasing threshold characteristics for devices from Y087L, similar to Y086L.

In pulsed operation (5kHz repetition rate and 1 μs pulse width), the Y087LBA1-1H and Y087LBA1-1F devices were able to lase up to 368 K and 369 K, with the results from Y087LBA1-1F shown in Fig. 11, which is also representative of the other devices tested. At their maximum operating temperature, these devices had emission wavelengths of 3.913 and 3.918 μm, and threshold current densities of J_{th} = 1120 and 1031.1 A/cm^2, respectively. At RT, these devices lased at 3.83 μm with threshold current densities of J_{th} = 162.7 and 151.1 A/cm^2, respectively. The devices from Y087L had emission wavelengths at RT that were red-shifted by a factor similar to the devices from Y086L. Their RT values of V_{th} = 3.34 and 3.39 V, respectively, lead to voltage efficiencies of about 58.2% and 57.4%. These results are slightly lower than those for devices from Y086L, but significantly higher than that for devices from Y082L. These results further suggest that the deviations from the design with increased layer thicknesses are less problematic in terms of carrier transport compared to the deviation scenario with reduced layer thickness. For devices from this ICL wafer, the T_o values ranged from 48.8 to 49.0 K in the temperature range of 200-360 K, which are comparable to those from the second ICL wafer, Y086L. Similar to devices from Y086L, those from Y087L had superior performance at 80 K compared to those from Y082L. At elevated temperatures beyond 300 K, both their J_{th} and V_{th} values exceeded those of devices from Y082L as reflected in Fig. 4, for reasons that are likely similar to those for Y086L, i.e., quickly increased free-carrier absorption loss at the more red-shifted wavelengths with increasing heat-sink temperature.

4 Conclusions

Three ICL wafers (Y082L, Y086L, and Y087L) each with the same 6-stage cascade active region design and with an advanced waveguide were grown by molecular beam epitaxy (MBE). Although there were significant deviations in layer thicknesses from the designed values, ICL devices made from the three wafers exhibited low threshold current densities at RT which are comparable to those in state-of-the-art ICLs at similar wavelengths. This suggests a promising potential for the advanced waveguide configuration to enhance the thermal and optical properties of ICLs. Also, a comparative study among the devices revealed that the decreased layer thicknesses due to growth deviations lead to a notable problem in the carrier transport that manifested in significantly higher

threshold voltages and low voltage efficiencies (<43%). Conversely, devices which had growth deviations with increased layer thicknesses had much less impact on the carrier transport, which is supported by high voltage efficiencies (e.g., 69%) and the higher cw operating temperature (e.g., 260 K) for BA devices from wafers Y086/87L. Such a high voltage efficiency (69%) is close to that (~70%) of state-of-the-art GaSb-based ICLs with the traditional waveguide. This implies that ICLs with the advanced waveguide configuration may achieve superior device performance when the structural deviations are minimized or the structure is optimized. Additionally, devices made from the ICL wafer Y082L demonstrated characteristic temperature even higher than state-of-the-art GaSb-based ICLs with the traditional waveguide, again suggesting considerable potential for GaSb-based ICLs with the advanced waveguide designed to operate at shorter wavelengths. Furthermore, this advanced waveguide configuration with the highly doped InAsSb outer cladding layer will be beneficial to lateral current conduction when the ICL structure is grown on a Si substrate [27], where the series resistance is significantly high through the InAs/AlSb SL cladding layer.

Data Availability Statement: The data that support these findings are available upon reasonable request from the authors.

Acknowledgements: This work was partially supported by NSF (No. ECCS-1931193) and OCAST (AR21-024).

References

1. R. Q. Yang, "Infrared laser based on intersubband transitions in quantum wells", Superlattices Microstruct., **17**, 77 (1995). [https://doi.org/10.1006/spmi.1995.1017]
2. R. Q. Yang, "Interband cascade (IC) lasers," in Semiconductor Lasers Fundamentals and Applications, edited by A. Baranov and E. Tournie (Woodhead Publishing, Cambridge, 2013), Chap. 12, pp. 487–513. [https://doi.org/10.1533/9780857096401.3.487]
3. J. Koeth, R. Weih, J. Scheuermann, M. Fischer, A. Schade, M. Kamp, and S. Höfling, "Mid infrared DFB interband cascade lasers," Proc. SPIE **10403**, 1040308 (2017). [https://doi.org/10.1117/12.2277698]
4. R. Q. Yang, L. Li, W. Huang, S. M. Shazzad Rassel, J. A. Gupta, A. Bezinger, X. Wu, G. Razavipour, and G. C. Aers, "InAs-based interband cascade lasers," IEEE J. Sel. Top. Quantum Electron. 25, 1200108 (2019). [10.1109/JSTQE.2019.2916923]

5. J. R. Meyer, W. W. Bewley, C. L. Canedy, C. S. Kim, M. Kim, C. D. Merritt, and I. Vurgaftman, "The interband cascade laser," Photonics **7**, 75 (2020). [https://doi.org/10.3390/photonics7030075]
6. J. Faist, F. Capasso, D. L. Sivco, C. Sirtori, A. L. Hutchinson, A. Y. Cho, "Quantum cascade laser," Science **264**, 553–556 (1994). [10.1126/science.264.5158.553]
7. I. Vurgaftman, P. Geiser, W. W. Bewley, C. D. Merritt, C. L. Canedy, M. V. Warren, M. Kim, C. S. Kim, and J. R. Meyer, "Sensitive chemical detection with distributed feedback interband Cascade lasers," in Encyclopedia of Analytical Chemistry, edited by R. A. Meyers (Wiley, Chichester, 2016). [https://doi.org/10.1002/9780470027318.a9559]
8. J. Scheuermann, P. Kluczynski, K. Siembab, M. Straszewski, J. Kaczmarek, et al, "Interband Cascade Laser Arrays for Simultaneous and Selective Analysis of C1–C5 Hydrocarbons in Petrochemical Industry", Applied Spectroscopy **75** (3), 336-342 (2021). [https://doi.org/10.1177/0003702820978231]
9. C. S. Goldenstein, R. M. Spearrin, J. B. Jeffries, and R. K. Hanson, "Infrared laser-absorption sensing for combustion gases," Prog. Energy Combust. Sci. **60**, 132–176 (2017). [https://doi.org/10.1016/j.pecs.2016.12.002]
10. A. Soibel, M. W. Wright, W. H. Farr, S. A. Keo, C. J. Hill, R. Q. Yang, and H. C. Liu, "Mid-infrared interband cascade laser for free space optical communication", IEEE Photonics Technol. Lett. **22**, 121 (2010). [10.1109/LPT.2009.2036449]
11. P. Didier, H. Knötig, O. Spitz, L. Cerutti, A. Lardschneider, E. Awwad, D. Diaz-Thomas, A. N. Baranov, R. Weih, J. Koeth, B. Schwarz, and F. Grillot, "Interband cascade technology for energy-efficient mid-infrared free-space communication," Photon. Res. **11**, 582-590 (2023).
12. H. Knotig, J. Nauschutz, N. Opacak, S. Hofling, J. Koeth, R. Weih, and B. Schwarz, "Mitigating valence intersubband absorption in interband cascade lasers", Laser & Photonics Reviews, 2200156 (2022).
13. J. Nauschutz, H. Knotig, R. Weih, J. Scheuermann, J. Koeth, S. Hofling, and B. Schwarz, "Pushing the room temperature continuous-wave operation limit of GaSb-based interband cascade lasers beyond 6 μm", Laser & Photonics Reviews, 2200587 (2023).
14. Z. Tian, R. Q. Yang, T. D. Mishima, M. B. Santos, R. T. Hinkey, M. E. Curtis, and M. B. Johnson, "InAs-based interband cascade lasers near 6 μm," Electron. Lett. **45**, 48 (2009). [10.1049/el:20092779]
15. Z. Tian, L. Li, H. Ye, R.Q. Yang, T.D. Mishima, M.B. Santos, and M.B. Johnson, "InAs-based interband cascade lasers with emission wavelengths at 10.4 μm," Electron. Lett. **48**, 113–114 (2012). [10.1049/el.2011.3555]
16. Lu Li, H. Ye, Y. Jiang, R. Q. Yang, J. C. Keay, T. D. Mishima, M. B. Santos, and M. B. Johnson, "MBE-grown long-wavelength interband cascade lasers on InAs substrates", Journal of Crystal Growth, **425**, 369 (2015). [https://doi.org/10.1016/j.jcrysgro.2015.02.016]
17. M. Dallner, F Hau, S Höfling, M Kamp, "InAs-based interband cascade lasers emitting around 7 μm with threshold current densities below 1 kA/cm^2 at room temperature", Appl. Phys. Lett., **106**, 041108 (2015). [https://doi.org/10.1063/1.4907002]
18. L. Li, Y. Jiang, H. Ye, R. Q. Yang, T. D. Mishima, M. B. Santos, and M. B. Johnson, "Low-threshold InAs-based interband cascade lasers operating at high temperatures," Appl. Phys. Lett. **106**, 251102 (2015). [https://doi.org/10.1063/1.4922995]
19. J. A. Massengale, Y. Shen, R. Q. Yang, S. D. Hawkins, and J. F. Klem, "Long wavelength interband cascade lasers," Appl. Phys. Lett. **120**, 091105 (2022). [https://doi.org/10.1063/5.0084565]
20. J. A. Massengale, Y. Shen, R. Q. Yang, S. D. Hawkins, and J. F. Klem, "Enhanced Performance of InAs-based Interband Cascade Lasers Emitting between 10-13 μm," Semiconductor Science and Technology **38**, 025009 (2022). [https://doi.org/10.1088/1361-6641/acac4e]
21. C. L. Canedy, M. V. Warren, C. D. Merritt, W. W. Bewley, C. S. Kim, M. Kim, I. Vurgaftman, and J. R. Meyer, "Interband cascade lasers with longer wavelengths," Proc. SPIE **10111**, 101110G (2017). [https://doi.org/10.1117/12.2246450]

22. Y. Lin, J. A. Massengale, W. Huang, R. Q. Yang, T. D. Mishima, M. B. Santos, “Examination of the Durability of Interband Cascade Lasers Against Structural Variations”, J. Infrared & Millimeter Waves. **39**, 137 (2020). [ISSN: 1001-9014]
23. J. A. Massengale, Y. Shen, R. Q. Yang, T. D. Mishima, Michael B. Santos, “GaSb-based interband cascade lasers with advanced waveguides operating near 3.3 and 3.4 μm”, *Proc. SPIE*. **12440**, 124400B (2023). [https://doi.org/10.1117/12.2647213]
24. I. Vurgaftman, R. Weih, M. Kamp, J. R. Meyer, C. L. Canedy, C. S. Kim, M. Kim, W. W. Bewley, C. D. Merritt, J. Abell, “Interband Cascade Lasers,” J. Phys. D: Appl. Phys. **48** 123001 (2015). [10.1088/0022-3727/48/12/123001]
25. R. Q. Yang, “Electronic States and Interband Tunneling Conditions in Type-II Quantum Well Heterostructures”, J. Appl. Phys. **127**, 025705 (2020).
26. R. Weih, M. Kamp, and S. Höfling, “Interband cascade lasers with room temperature threshold current densities below 100 A/cm^2,” Appl. Phys. Lett. **102**, 231123 (2013). [https://doi.org/10.1063/1.4811133]
27. Laurent Cerutti, Daniel A. Díaz Thomas, Jean-Baptiste Rodriguez, Marta Rio Calvo, Gilles Patriarche, Alexei N. Baranov, and Eric Tournié, "Quantum well interband semiconductor lasers highly tolerant to dislocations," Optica **8**, 1397-1402 (2021).

Jeremy Massengale received his Ph.D. degree in 2023 in physics from the University of Oklahoma where he worked with Dr. Rui Yang and Dr. Michael Santos on the growth, fabrication, and characterization of interband cascade based mid-IR devices. He currently holds a National Research Council post-doctoral fellowship at the US Naval Research Laboratory. His research interests include the development of growth techniques for III-V based superlattice structures, XRD characterization, nanofabrication methods, and optical characterization techniques for mid-IR devices.

Yixuan Shen received his B.S. degree in electrical engineering and automation from Shanghai Ocean University in 2016 and his M.S. degree in electrical engineering from the University of Oklahoma in 2023. He is currently pursuing his Ph.D. degree in electrical engineering at the University of Oklahoma, where he works with Dr. Rui Yang and Dr. Michael Santos on interband cascade laser research. His research focuses on optimizing the waveguide structure of mid-IR interband cascade lasers with III-V materials.

Rui Q. Yang received his Ph.D. degree in 1987 in physics from Nanjing University with research activities ranging from physics to semiconductor quantum devices. He has authored/co-authored more than 150 refereed journal articles and two book chapters with 11 patents. He is a Fellow of IEEE and Optica and received the 2018 IEEE Photonics Society Aron Kressel Award for the invention of the mid-infrared interband cascade laser, and its advancement along with related devices for applications.

Tetsuya D. Mishima received his Ph.D. degree from Waseda University, Tokyo, Japan, in 1999. He has been a Research Scientist with the University of Oklahoma, Norman, since 2001. He previously held a post-doctoral position at Pennsylvania State University, University Park, from 1999 to 2001. His current research interests include structural defect reduction in semiconductor structures grown by molecular beam epitaxy, development of transmission electron microscopy

techniques for structural defect analysis, and theoretical analysis on carrier transport in quantum well structures.

Michael B. Santos received his B.S. degree in electrical engineering and materials science from Cornell University, Ithaca, NY, and his Ph.D. degree in electrical engineering from Princeton University, Princeton, NJ, in 1986 and 1992, respectively. He was a Post-Doctoral Researcher with AT&T Bell Laboratories, Holmdel, NJ, before joining the University of Oklahoma, Norman, in 1993. He is currently a Professor of Physics with the University of Oklahoma. He has co-authored 270 papers on experimental semiconductor research.

Figure Caption List:

Fig. 1a. A schematic diagram of the overall structure showing the various waveguide segments and the cascade active region, as well as connection regions (hatched) between them.

Fig. 1b. The experimentally measured XRD pattern (blue) along with the simulated pattern (red) for Y082L, which is representative of all ICL wafers grown. The origin for the x-axis is at the (004) peak for the GaSb substrate.

Fig. 2. The calculated optical modal profile and refractive index for the ICL based on the intended design parameters. Listed in the plot are the optical confinement factor (Γ), the internal loss due to free-carrier absorption (α_i), and the effective refractive index (n_{eff}).

Fig. 3. The calculated optical modal profile and refractive index for Y082L (red) and Y086L (green) based on the intended operating wavelength, but with the structure thicknesses modified by the measured XRD results.

Fig. 4. The measured threshold current density (J_{th}) and threshold voltage (V_{th}) as a function of temperature for several devices from the three ICL wafers in both cw (solid) and pulsed (dashed) operation.

Fig. 5. The cw and pulsed emission wavelengths as functions of heat-sink temperature. Also shown are the average red-shift of the emission wavelength per unit heat-sink temperature.

Fig. 6. The CW IVL characteristics for Y082LBA1-3F from 80 K to its 240 K along with the corresponding EQE values.

Fig. 7. The pulsed lasing spectra for Y082LBA1-3F along with the threshold current density, threshold voltage, and emission wavelength at each temperature step.

Fig. 8. The CW IVL characteristics for Y086LBA1-2B from 80 K to 240 K along with the corresponding EQE values.

Fig.9. The pulsed spectra (Y086LBA1-1H) along with the threshold current density, threshold voltage, and emission wavelength at each temperature step.

Fig. 10. The CW IVL characteristics for Y087LBA1-1H from 80 K to 250 K along with the corresponding EQE values.

Fig. 11. The pulsed spectra (Y087LBA1-1F) along with the threshold current density, threshold voltage, and emission wavelength at each temperature step.

Figures

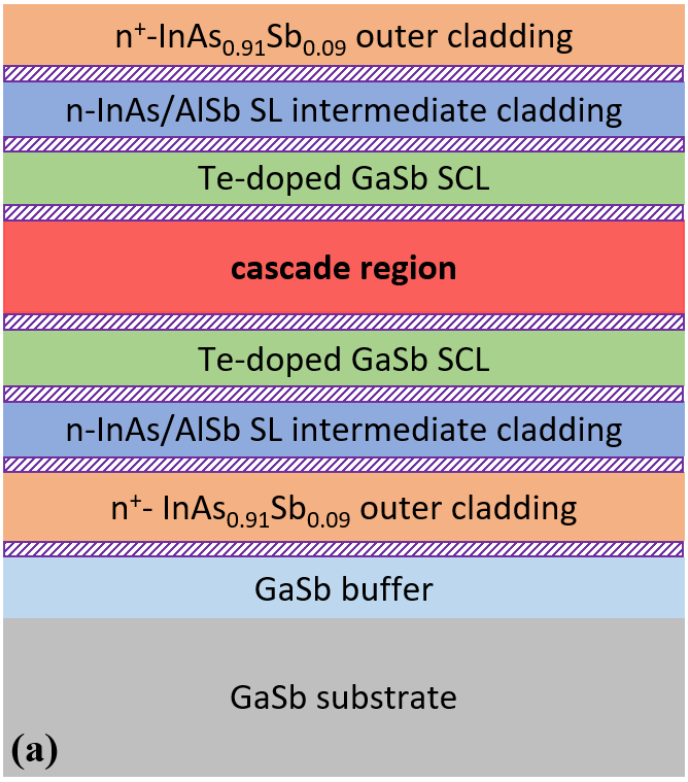

Fig. 1a

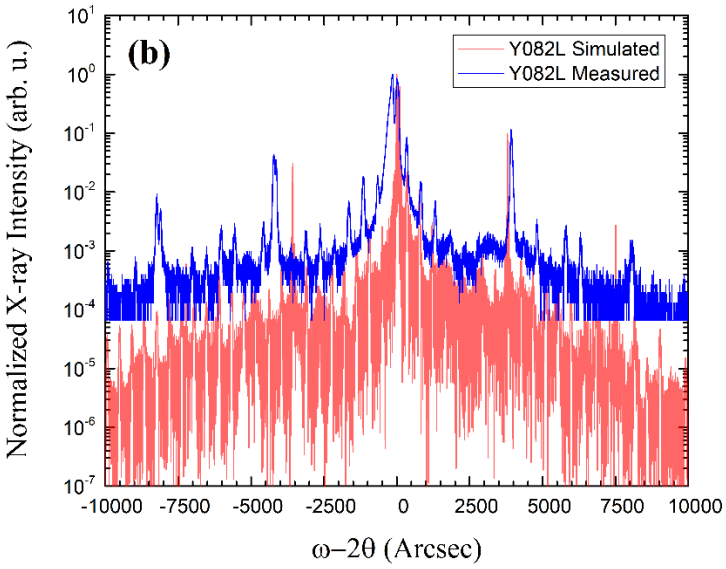

Fig. 1b

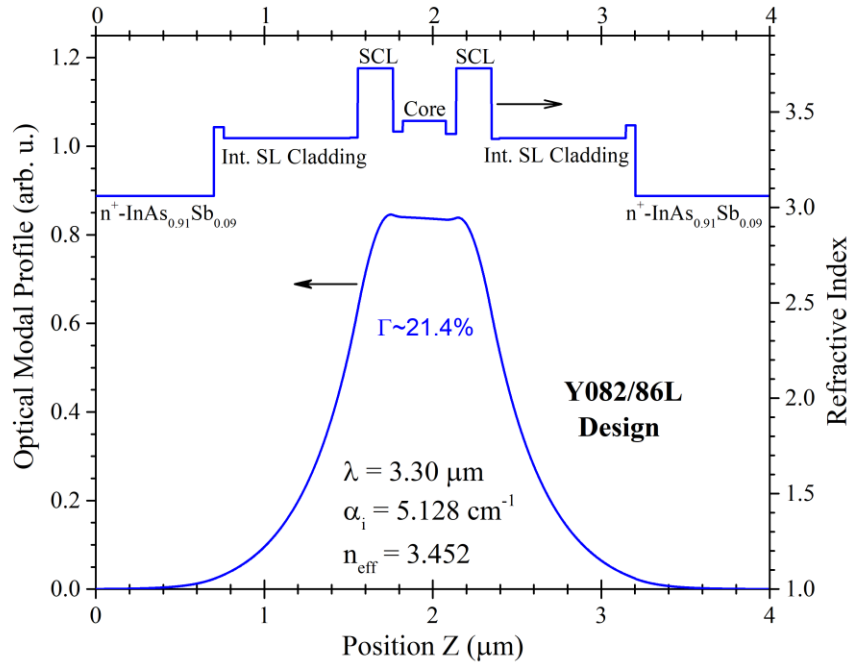
SCL
SCL
Core
Int. SL Cladding
Int. SL Cladding
n+-InAs0.91Sb0.09
n+-InAs0.91Sb0.09
Γ~21.4%
Y082/86L
Design
λ = 3.30 μm
αi = 5.128 cm-1
neff = 3.452
Optical Modal Profile (arb. u.)
Refractive Index
Position Z (μm)

Fig. 2

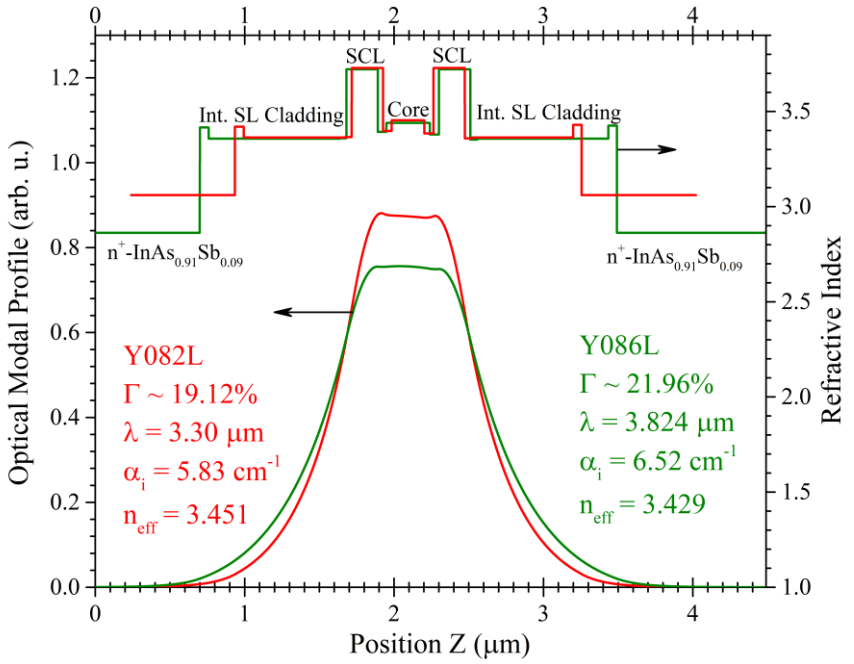
SCL
SCL
Int. SL Cladding
Core
Int. SL Cladding
n+-InAs0.91Sb0.09
n+-InAs0.91Sb0.09
Y082L
Γ ~ 19.12%
λ = 3.30 μm
αi = 5.83 cm-1
neff = 3.451
Y086L
Γ ~ 21.96%
λ = 3.824 μm
αi = 6.52 cm-1
neff = 3.429
Optical Modal Profile (arb. u.)
Refractive Index
Position Z (μm)

Fig.3

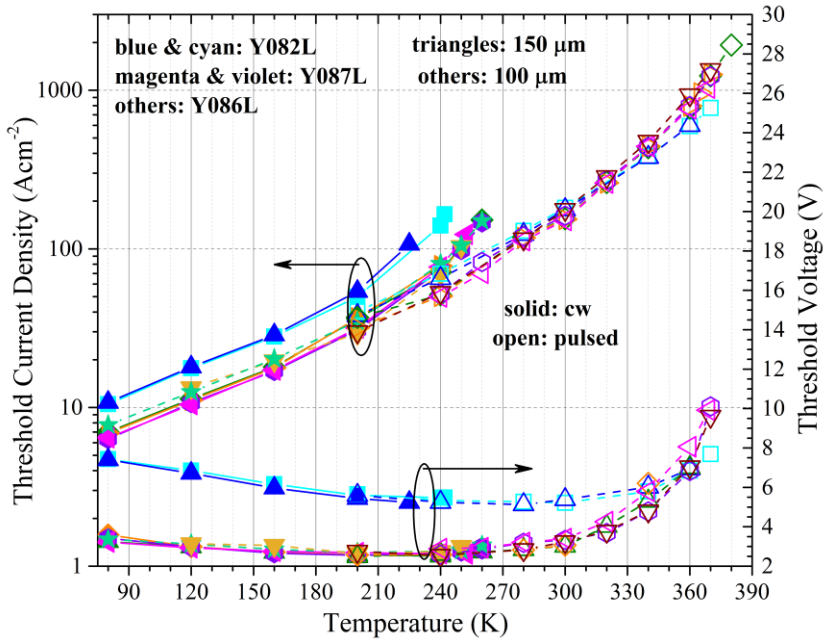
blue & cyan: Y082L
magenta & violet: Y087L
others: Y086L
triangles: 150 μm
others: 100 μm
solid: cw
open: pulsed
Threshold Current Density (Acm-2)
Threshold Voltage (V)
Temperature (K)

Fig.4

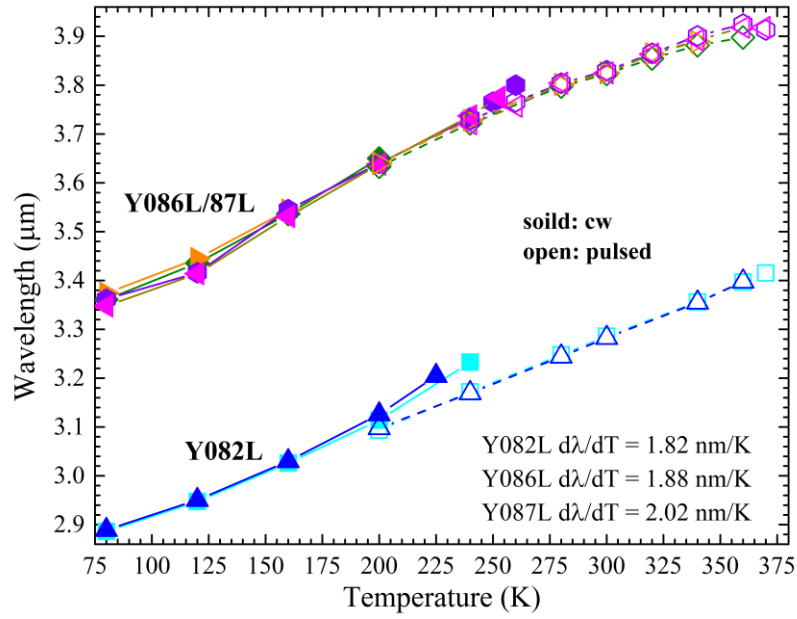
Y086L/87L
soild: cw
open: pulsed
Y082L
Y082L dλ/dT = 1.82 nm/K
Y086L dλ/dT = 1.88 nm/K
Y087L dλ/dT = 2.02 nm/K
Wavelength (μm)
Temperature (K)

Fig. 5

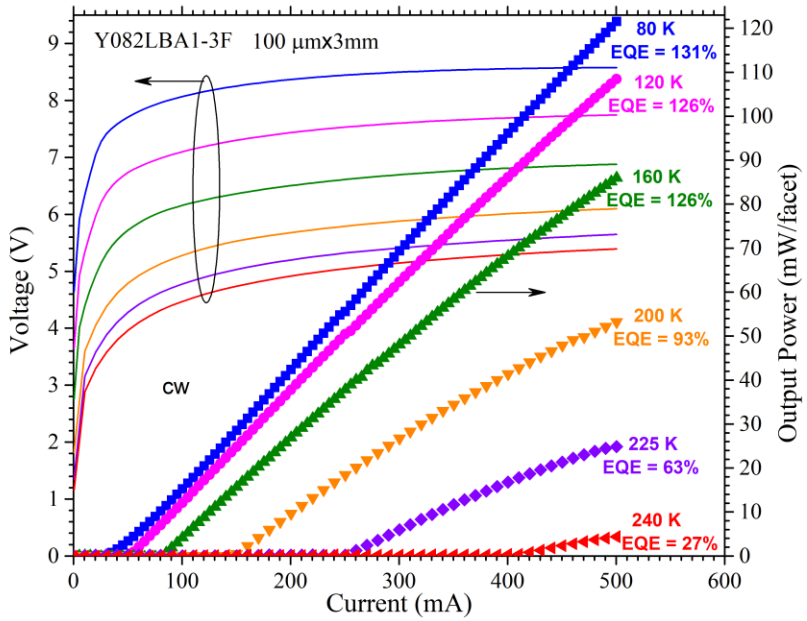
Y082LBA1-3F 100 µmx3mm
80 K
EQE = 131%
120 K
EQE = 126%
160 K
EQE = 126%
200 K
EQE = 93%
225 K
EQE = 63%
240 K
EQE = 27%
cw
Voltage (V)
Output Power (mW/facet)
Current (mA)

Fig. 6

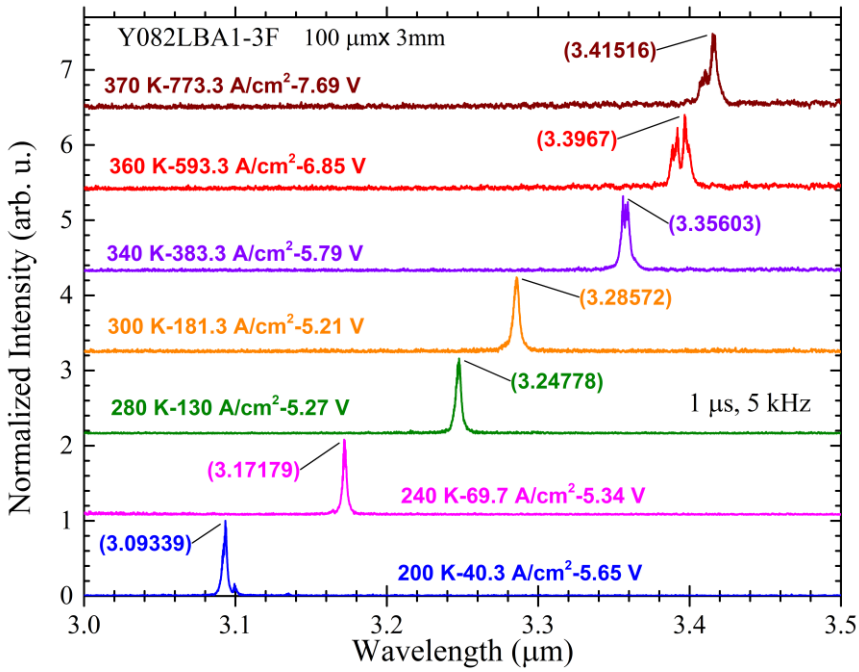
Y082LBA1-3F 100 µmx 3mm
(3.41516)
370 K-773.3 A/cm²-7.69 V
(3.3967)
360 K-593.3 A/cm²-6.85 V
(3.35603)
340 K-383.3 A/cm²-5.79 V
(3.28572)
300 K-181.3 A/cm²-5.21 V
(3.24778)
280 K-130 A/cm²-5.27 V
1 µs, 5 kHz
(3.17179)
240 K-69.7 A/cm²-5.34 V
(3.09339)
200 K-40.3 A/cm²-5.65 V
Normalized Intensity (arb. u.)
Wavelength (µm)

Fig. 7

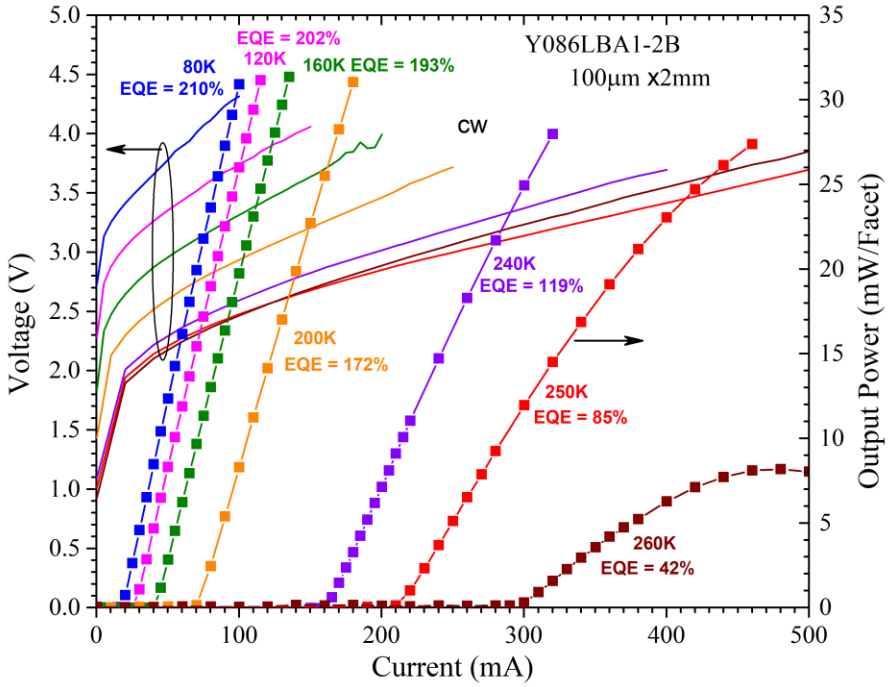
Y086LBA1-2B
100μm x2mm
80K
EQE = 210%
EQE = 202%
120K
160K EQE = 193%
CW
240K
EQE = 119%
200K
EQE = 172%
250K
EQE = 85%
260K
EQE = 42%
Voltage (V)
Output Power (mW/Facet)
Current (mA)

Fig. 8

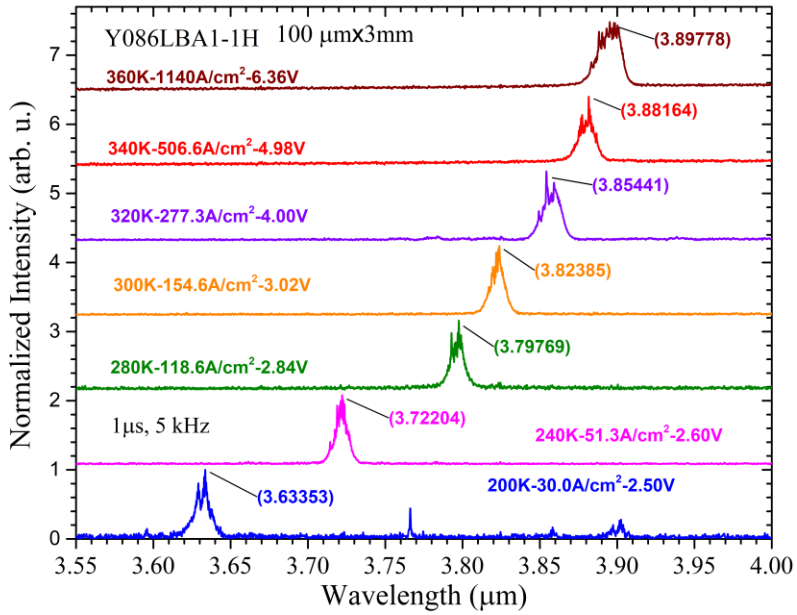
Y086LBA1-1H 100 μmx3mm
360K-1140A/cm²-6.36V
(3.89778)
340K-506.6A/cm²-4.98V
(3.88164)
320K-277.3A/cm²-4.00V
(3.85441)
300K-154.6A/cm²-3.02V
(3.82385)
280K-118.6A/cm²-2.84V
(3.79769)
1μs, 5 kHz
(3.72204)
240K-51.3A/cm²-2.60V
200K-30.0A/cm²-2.50V
(3.63353)
Normalized Intensity (arb. u.)
Wavelength (μm)

Fig. 9

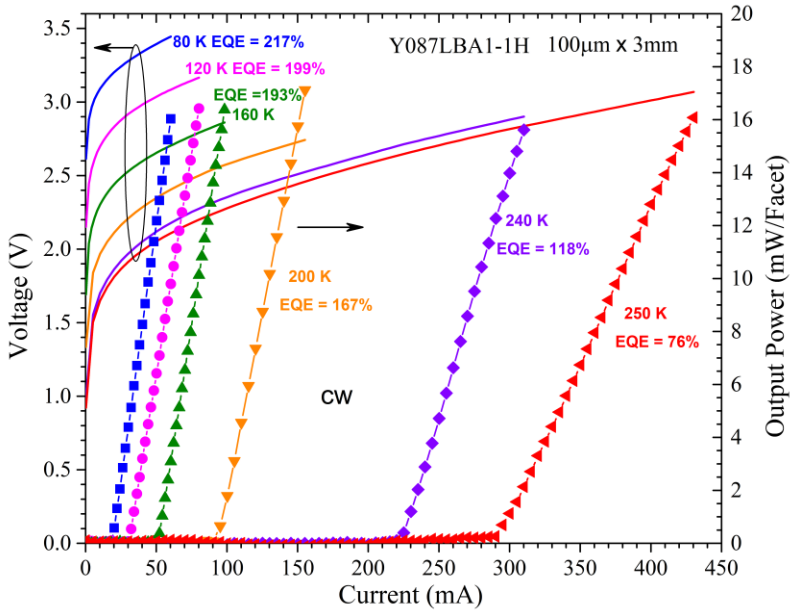
Y087LBA1-1H 100μm x 3mm
80 K EQE = 217%
120 K EQE = 199%
EQE =193%
160 K
200 K
EQE = 167%
240 K
EQE = 118%
250 K
EQE = 76%
CW
Voltage (V)
Output Power (mW/Facet)
Current (mA)

Fig. 10

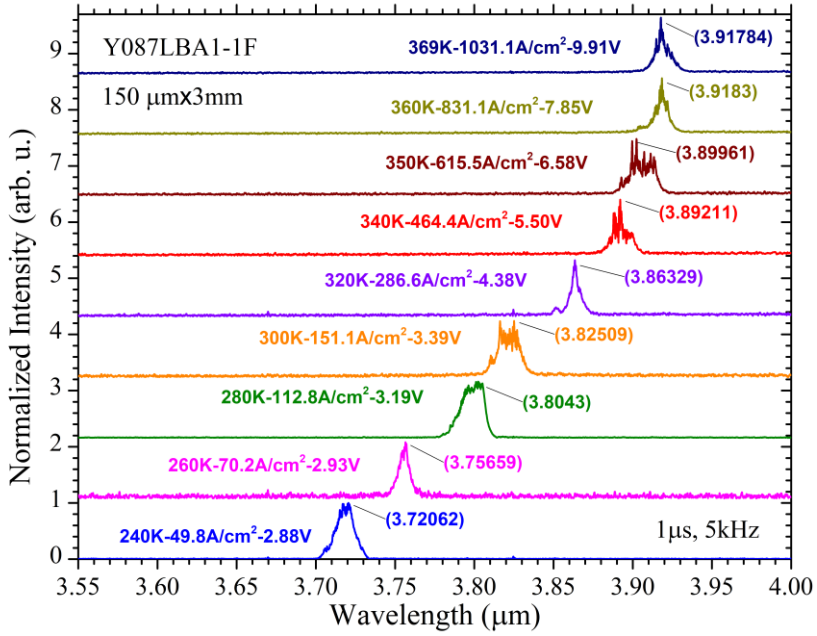
Y087LBA1-1F
150 μmx3mm
369K-1031.1A/cm²-9.91V
(3.91784)
360K-831.1A/cm²-7.85V
(3.9183)
350K-615.5A/cm²-6.58V
(3.89961)
340K-464.4A/cm²-5.50V
(3.89211)
320K-286.6A/cm²-4.38V
(3.86329)
300K-151.1A/cm²-3.39V
(3.82509)
280K-112.8A/cm²-3.19V
(3.8043)
260K-70.2A/cm²-2.93V
(3.75659)
240K-49.8A/cm²-2.88V
(3.72062)
1μs, 5kHz
Normalized Intensity (arb. u.)
Wavelength (μm)

Fig. 11